Spin and orbital disordering by hole doping in $Pr_{1-x}Ca_xVO_3$

M. Reehuis,[1] C. Ulrich,[2,3] P. M. Abdala,[4] P. Pattison,[4,5] G. Khaliullin,[6] J. Fujioka,[7] S. Miyasaka,[7] Y. Tokura,[7,8] and B. Keimer[6]

[1]*Helmholtz-Zentrum Berlin für Materialien und Energie, D-14109 Berlin, Germany*

[2]*School of Physics, The University of New South Wales, Sydney, NSW 2052, Australia*

[3]*Australian Nuclear Science and Technology Organisation, Lucas Heights, NSW 2234, Australia*

[4]*Swiss-Norwegian Beamline (SNBL) at the European Synchrotron Radiation Facility (ESRF), BP 220, F-38042 Grenoble Cedex 9, France*

[5]*Laboratory of Crystallography, École Polytechnique Fédérale de Lausanne (EPFL), BSP-Dorigny, CH-1015 Lausanne, Switzerland*

[6]*Max-Planck-Institut für Festkörperforschung, D-70569 Stuttgart, Germany*

[7]*Department of Applied Physics, University of Tokyo, 113-8656 Tokyo, Japan*

[8]*Correlated Electron Research Center (CERC), National Institute of Advanced Industrial Science and Technology (AIST), Tsukuba 305-8562, Japan*

(Received 13 May 2016; revised manuscript received 30 July 2016; published 29 September 2016)

High-resolution powder x-ray diffraction and single-crystal neutron diffraction were used to investigate the crystal structure and magnetic ordering of the compound $Pr_{1-x}Ca_xVO_3$ ($0 \leqslant x \leqslant 0.3$), which undergoes an insulator-to-metal transition for $x \sim 0.23$. Since the ionic radii of Pr^{3+} and Ca^{2+} are almost identical and structural disorder is minimal, $Pr_{1-x}Ca_xVO_3$ is a good model system for the influence of hole doping on the spin and orbital correlations in transition metal oxides. The end member $PrVO_3$ is a Mott-Hubbard insulator, which exhibits a structural phase transition at $T_S = 180$ K from an orthorhombic to a monoclinic structure with space groups *Pbnm* and $P2_1/b$, respectively. This transition is associated with the onset of orbital ordering and strong Jahn-Teller distortions of the VO_6 octahedra. Antiferromagnetic C-type order with vanadium moments oriented in the ab plane is observed below $T_N = 140$ K. Upon cooling, the vanadium moments induce a progressive magnetic polarization of the praseodymium sublattice, resulting in a ferrimagnetic structure with coexisting modes (C_x, F_y) and (F_x, C_y). In the insulating range of the $Pr_{1-x}Ca_xVO_3$ phase diagram, Ca doping reduces both the orbital and magnetic transition temperatures so that $T_S = 108$ K and $T_N = 95$ K for $x = 0.20$. The Jahn-Teller distortions and ordered vanadium moments also decrease upon doping. In a metallic sample with $x = 0.30$, Jahn-Teller distortions and long-range orbital ordering are no longer observable, and the average crystal structure remains orthorhombic down to low temperature. However, broadening of some lattice Bragg reflections indicate a significant increase in lattice strain. Antiferromagnetic short-range order with a weak ordered moment of 0.14(3) μ_B per vanadium atom could still be observed on the vanadium site below $T \sim 60$ K. We discuss these observations in terms of doping-induced spin-orbital polaron formation.

DOI: 10.1103/PhysRevB.94.104436

I. INTRODUCTION

Perovskites with a cubic (or nearly cubic) crystal structure built up of metal-oxide octahedra exhibit intriguing phenomena such as insulator-to-metal transitions (IMTs) and colossal magnetoresistance, which originate in interdependent charge, spin, and orbital correlations of the strongly correlated d electrons residing on the metal ions. The influence of the orbital degrees of freedom of the d electrons on the magnetic and transport properties of metal-oxide compounds has attracted much attention in recent years [1]. Mott-insulating orthovanadates of chemical composition RVO_3 (R = Y or a trivalent rare-earth metal) have been widely studied as a model system of the coupling between the spin and orbital degrees of freedom [2–18]. The valence electrons on the V^{3+} ions (electron configuration $3d^2$) reside in the t_{2g} manifold of the nearly cubic crystal field, which exhibits a significantly lower energy level splitting than the e_g manifold that accommodates the valence electrons in the isostructural manganates. Since the energy separation of the orbital levels is comparable to the spin interactions, the insulating vanadates undergo multiple magnetic and orbital ordering transitions and are believed to exhibit strong spin-orbital fluctuations [2,3,19,20].

At room temperature, the orthovanadates crystallize in the orthorhombic $GdFeO_3$-type structure with space group *Pbnm* [21–24]. With decreasing temperature, they undergo a structural phase transition at $T_S \sim 150$–200 K into a monoclinic phase described by the space group $P2_1/b$. This transition is associated with Jahn-Teller distortions in the VO_6 octahedra (Fig. 1) and can be attributed to the onset of orbital ordering. Upon further cooling, a Néel transition occurs at $T_N \sim 100$–140 K due to the formation of a C-type magnetic structure of the spin-1 moments of V^{3+}. This phase was attributed to an orbital Peierls state driven by one-dimensional spin-orbital fluctuations [3]. For vanadates containing R^{3+} ions smaller than Dy^{3+}, including in particular the extensively investigated YVO_3, a second structural transition back to the orthorhombic space group *Pbnm* was found below ~77 K. In this low-temperature phase, a rearrangement of the magnetic moments into a G-type structure as well as a change to a C-type orbital order was observed. The spin and orbital ordering transitions are associated with unusual macroscopic properties such as a temperature-induced magnetization reversal and a magnetic memory effect observed in YVO_3 [4]. The evolution of spin-orbital-lattice coupling in RVO_3 perovskites was described in a microscopic spin-orbital model, where the ionic radius $r(R^{3+})$ affects the V-O-V bonds and hence the orbital-dependent superexchange interactions between the vanadium spins [25].

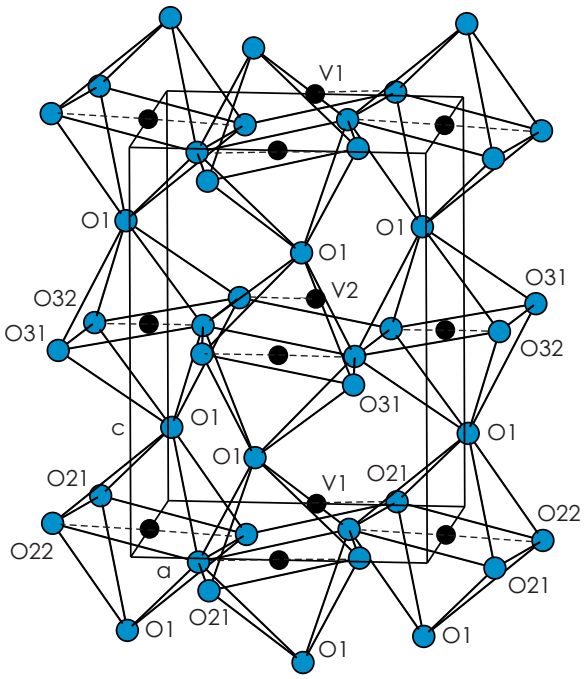

FIG. 1. Network of distorted corner-sharing VO_6 octahedra in the monoclinic structure ($P2_1/b$) of $PrVO_3$ at 15 K. The dashed lines represent the elongated V-O bonds due to the Jahn-Teller effect.

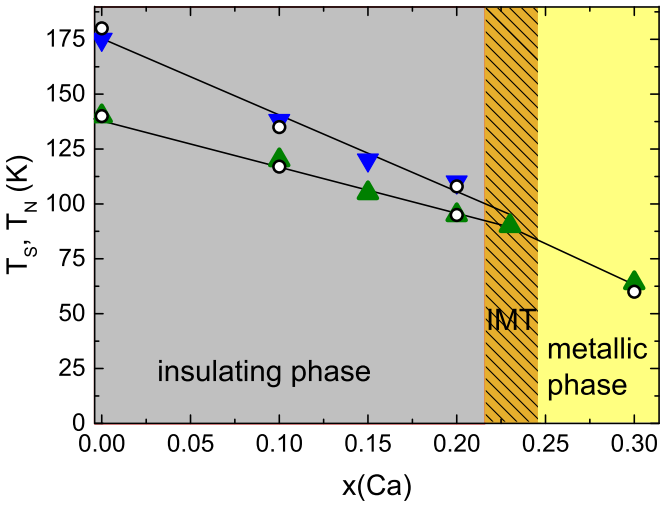

FIG. 2. Change of the structural and magnetic phase transitions in the system $Pr_{1-x}Ca_xVO_3$ as a function of the doping level x. With increasing Ca content, an IMT occurs at $x = 0.23$, which causes the melting of the G-type orbital order. The structural and magnetic phase transitions were determined earlier from specific heat (blue triangles) and magnetization measurements (green triangles), respectively [10]. In the present paper, both types of phase transitions were reinvestigated by single-crystal neutron diffraction (open black circles). Note that the error bars correspond to the size of the symbols. The bold lines are guides to the eye.

In this paper, we focus on the influence of hole doping on the microscopic spin and orbital correlations in $Pr_{1-x}Ca_xVO_3$, following up on prior work on the doping dependence of the macroscopic magnetic, optical, and transport properties of $Pr_{1-x}Ca_xVO_3$, as well as other hole-doped vanadates, including $La_{1-x}Sr_xVO_3$, $Nd_{1-x}Sr_xVO_3$, and $Y_{1-x}Ca_xVO_3$ [8–13]. In general, the partial replacement of the R^{3+} ions by divalent alkaline-earth ions $A^{2+} = Ca^{2+}$ or Sr^{2+} induces holes in the t_{2g} electronic level of the V^{3+} ions. In addition, modifications of the one-electron bandwidth through changes in the crystal structure induced by chemical substitution are also expected (Refs. [8–13] and [26]), and the substitutional disorder can strongly affect the transport and optical properties [27–30]. Calcium doped $PrVO_3$ can be considered as a special case because the ionic radii of Pr^{3+} (1.126 Å) and Ca^{2+} (1.120 Å) are almost identical (see Ref. [31]), so that structural disorder is expected to be minimal. Figure 2 shows that the increase of the doping level x in $Pr_{1-x}Ca_xVO_3$ causes a decrease of both structural and magnetic transition temperatures, which was ascribed to a gradual melting of the spin and the orbital order [10]. Further doping to $x \sim 0.23$ results in a doping-induced insulator-metal transition (IMT) [10].

The critical doping level of the IMT in the doped vanadates (between $x = 0.178$ and 0.5 for the systems mentioned above) is significantly larger than the value expected for an orbitally nondegenerate doped Mott insulator (e.g., the layered cuprates with $x \sim 0.05$). Therefore, orbital correlations must be involved in the dynamics of the charge carriers. Indeed, the IMT in $Pr_{1-x}Ca_xVO_3$ is accompanied by a melting of the orbital order (see Ref. [10]), which underlines the importance of orbital correlations in this system. However, earlier studies did not give a detailed description of changes in the crystal structure and the magnetic ordering pattern of hole-doped vanadates from the insulating to the metallic state. A charge carrier doped in a Mott insulator with orbital degeneracy can locally modify the orbital structure and covalent bonding, which also affects the spin and lattice degrees of freedom through the orbital-spin and orbital-lattice coupling. The resulting complex object—a spin-orbital polaron—may have a large effective mass, which reduces its mobility. This enhances localization effects and results in a self-trapping of the charge carriers in the random potential of the dopant ions. At large doping levels, the spin-orbital polaron binding energy decreases, resulting in a transition to coherent metallic state [32]. One may thus expect changes in the x-ray and neutron diffraction patterns across the IMT.

Motivated by these findings and predictions, we have carried out a systematic investigation of the doping dependence of the crystal and magnetic structure of $Pr_{1-x}Ca_xVO_3$ by high-resolution synchrotron x-ray powder diffraction and single-crystal neutron diffraction. In the insulating phase, a continuous decrease of both the structural and the magnetic phase transition temperature with increasing doping level is confirmed. In the metallic phase, the long-range orbital order is quenched, but strongly anisotropic lattice strains presumably associated with short-range orbital correlations persist. Weak antiferromagnetic short-range order of the vanadium moments is also observed below ~60 K. Our combined x-ray and neutron diffraction investigation therefore points towards a strong involvement of spin-orbital polarons in the IMT in $Pr_{1-x}Ca_xVO_3$.

II. EXPERIMENTAL DETAILS

In order to investigate the doping dependent structural properties of $Pr_{1-x}Ca_xVO_3$, we performed high-resolution synchrotron powder diffraction studies at the beam lines BM1A and BM1B (Swiss-Norwegian) at the ESRF in Grenoble. The x-ray wavelengths were $\lambda = 0.6976$ Å and $\lambda = 0.5037$ Å, respectively. For the experiment, we ground single crystals of pure $PrVO_3$ and hole-doped vanadates with $x = 0.10, 0.15, 0.20$, and 0.30 to a powder, which was mounted in a glass capillary of diameter 0.5 mm. Complete powder patterns of each sample were collected at 15 and 295 K in a 2θ-range between 1 and 55°. Rietveld refinements of the powder diffraction data were carried out with the program FullProf, using the atomic scattering factors provided by this program [33].

The magnetic structures in $Pr_{1-x}Ca_xVO_3$ were investigated up to a doping level $x = 0.30$ by single-crystal neutron diffraction on the instrument E5 at the BER II reactor of the Helmholtz-Zentrum Berlin. A pyrolytic-graphite monochromator was used to select the neutron wavelength $\lambda = 2.36$ Å. For the experiment, we used cylindrical single crystals with dimensions $d = 3$–4 mm and $h = 3$–6 mm, which were grown by a floating-zone method, as described elsewhere [8,9]. For the determination of the magnetic moments, we needed to determine the overall scale factor from sets of nuclear reflections of the orthorhombic phase collected well above the structural phase transition T_S. Therefore, for each vanadate, a total number of about 80 Bragg reflections (35 unique) was collected at 190 K ($PrVO_3$), at 160 K ($Pr_{0.90}Ca_{0.10}VO_3$), and at 150 K ($Pr_{0.80}Ca_{0.20}VO_3$ and $Pr_{0.70}Ca_{0.30}VO_3$), respectively. Data reduction and crystal structure refinements were carried out with the program Xtal 3.4 [34]. For the absorption correction, we used the absorption coefficient $\mu = 0.79\,\mathrm{cm}^{-1}$. The absorption-weighted mean path lengths through the sample were used for the extinction correction for all individual reflections. We applied the method of Zachariasen (Gaussian mosaic-spread distribution). For the crystal structure refinements, we used the nuclear scattering lengths $b(\mathrm{O}) = 5.805$ fm, $b(\mathrm{Ca}) = 4.90$ fm, $b(\mathrm{V}) = -0.3824$ fm, and $b(\mathrm{Pr}) = 4.45$ fm [35]. The magnetic moments of the V and Pr atoms were refined with the program FullProf (see Ref. [33]), where the magnetic form factors of the metal ions were taken from Ref. [36].

III. RESULTS AND DISCUSSION

A. Structural and magnetic phase transitions

The phase diagram for $Pr_{1-x}Ca_xVO_3$ has already been studied by transport, specific heat, and magnetization measurements (see Ref. [10]), which revealed both structural and magnetic phase transitions (Fig. 2). In the present paper, we have performed single-crystal neutron diffraction experiments to investigate these transitions by measuring the temperature dependence of corresponding Bragg reflections. In earlier studies of insulating vanadates, the structural phase transition temperatures were extracted from intensity changes of strong nuclear Bragg reflections [3,15–17]. Due to the spontaneous onset of orbital ordering, which is accompanied by Jahn-Teller distortions in the VO_6 octahedra, the crystal structure changes upon cooling from an orthorhombic to a monoclinic structure (see Sec. III B below). Changes in the intensities of strong Bragg peaks in a single crystal, which are affected by self-extinction effects, can be ascribed to changes of the mosaicity of the crystal. Accordingly, the structural phase transition temperature in $Pr_{1-x}Ca_xVO_3$ can be accurately extracted from the temperature dependence of the intensities of the reflection 022 (Fig. 3). For the end member $PrVO_3$, the structural transition was found at $T_S = 180(2)$ K. With increasing Ca content up to $x = 0.20$, one finds a strong decrease of the transition temperature down to $T_S = 108(2)$ K, indicating a destabilization of the orbitally ordered state (Fig. 2). The results are in good agreement with those obtained by specific-heat measurements carried out earlier [10]. Further increasing the Ca content up to $x = 0.23$ results in a transition from the insulating to the metallic state. For the metallic vanadate $Pr_{0.70}Ca_{0.30}VO_3$, no anomaly in the Bragg peak intensities akin to those in the insulating state could be detected down to the lowest temperature, indicating a quenching of long-range orbital ordering.

The strongest magnetic intensity was observed on the position of the reflection 100, which corresponds to $^1/_2{}^1/_2 0$ in the pseudo-cubic notation. This Bragg reflection can be attributed to the C-type magnetic ordering of the vanadium sublattice (Fig. 3). For the end member $PrVO_3$, the magnetic order sets in at the Néel temperature $T_N = 140(2)$ K. With increasing doping level up to $x = 0.20$, the transition temperature decreases to $T_N = 95(2)$ K, indicating a destabilization of the C-type antiferromagnetic ordering, in a manner similar to the observed destabilization of the G-type orbital ordering. Due to the quenching of the orbital order in the metallic phase, one might expect that the C-type spin ordering would also be completely quenched. However, we still found a weak magnetic contribution on the reflection 100 for metallic $Pr_{0.70}Ca_{0.30}VO_3$ below a temperature of about 60 K (Fig. 3). This is in agreement with specific heat and magnetization measurements, where weak anomalies were also found at this temperature for this sample [10].

Upon further cooling, the intensity of the 100 C-type antiferromagnetic reflection of both insulating and metallic vanadates first show a maximum followed by a continuous decrease of the magnetic intensity (Fig. 3). This behavior was also observed for $CeVO_3$ and $TbVO_3$, where it was ascribed to the influence of the lanthanide moments, which become polarized in the presence of the exchange field produced by the antiferromagnetic vanadium sublattice [15,16]. A detailed description of the magnetic ordering pattern of $Pr_{1-x}Ca_xVO_3$ is given in Sec. III C.

B. Influence of Ca doping on the crystal structure

In order to determine the doping dependent crystal structure in $Pr_{1-x}Ca_xVO_3$, we have carried out a high-resolution synchrotron x-ray powder diffraction study of a series of samples with $0 \leqslant x \leqslant 0.30$. Measurements were performed in the monoclinic phase at $T = 15$ K and in the orthorhombic phase at 295 K. For both phases, the increasing Ca content results in systematic shifts of the peak positions of both 022 and 202 Bragg reflections to higher scattering angles, indicating a shortening of the lattice parameters (Fig. 4). From our

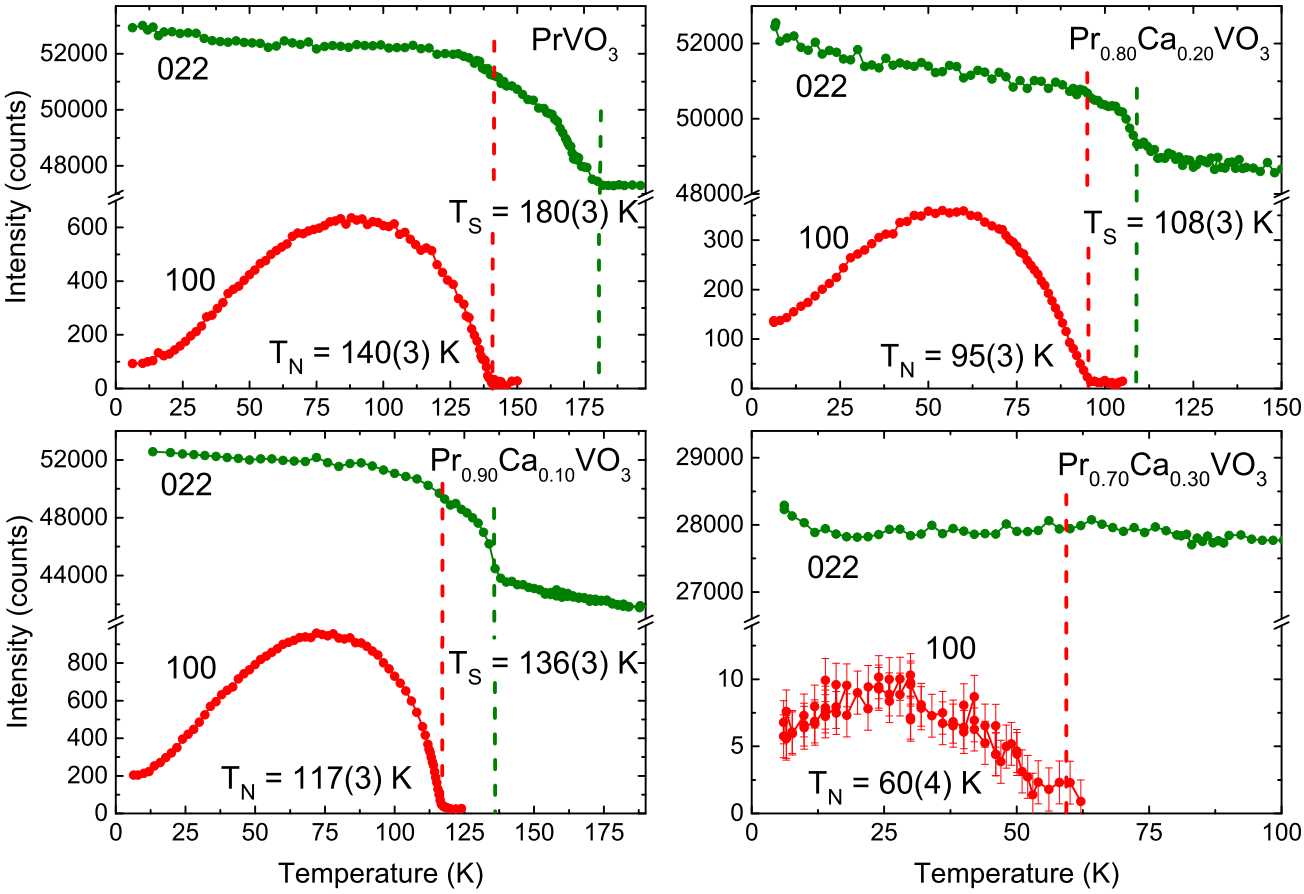

FIG. 3. Temperature dependence of the magnetic 100 (red) and nuclear 022 (green) Bragg intensities of $Pr_{1-x}Ca_xVO_3$. For the insulating vanadates ($x \leqslant 0.23$) anomalies were observed for the nuclear reflection 022 indicating a structural phase transition from the orthorhombic (*Pbnm*) to the monoclinic ($P2_1/b$) structure. The spontaneous increase of the intensity of the reflection 100 shows the onset of *C*-type spin ordering of the vanadium sublattice.

Rietveld refinements, the lattice parameters *a*, *b*, and *c* could be determined with high accuracy (Table I). At 295 K, all three lattice parameters of the orthorhombic phase show almost the same linear decrease from the insulating to the metallic state (Fig. 5) so that the cell volume is reduced by 2.8%. Within the monoclinic phase at 15 K, the doping-induced reduction of the cell volume (3.1%) is similar to the value determined at 295 K, but the decrease of the *b* axis is larger than that of the *c* axis, indicating the presence of Jahn-Teller distortions of the VO_6 octahedra. Usually a change of the lattice parameters is strongly influenced by the ionic size and the valence of the R^{n+} ions, as shown earlier for rare-earth vanadates RVO_3 [15–18]. In the system $Pr_{1-x}Ca_xVO_3$, the influence of the ionic size effect at the *R* site should be negligible since the ionic radii of Pr^{3+} and Ca^{2+} are almost identical (see Ref. [31]). The continuous reduction of all lattice parameters is presumably driven by the shortening of the V-O-bond lengths (Table I), which can be ascribed to the increasingly covalent character of the V-O bonds in the hole-doped vanadates (where the holes mostly reside in oxygen *p* orbitals) and/or the enhanced Coulomb attraction between V and O ions.

We now discuss the structural changes from the insulating to the metallic state, beginning with the data at room temperature, where Jahn-Teller distortions (associated with orbital order) and magnetoelastic effects (associated with magnetic order) are absent. From the data sets collected at 295 K, we found that the crystal structure of all samples can be described in the orthorhombic space group *Pbnm* (standard setting *Pnma*, No. 62). The principal cause of the deviations from the ideal perovskite structure is tilting of the VO_6 octahedra, which are more strongly rotated around the *b* and *c* axes than around *a*. Rietveld refinements of the synchrotron powder patterns resulted in satisfactory residuals of $R_F \leqslant 0.026$. In the space group *Pbnm*, the vanadium atoms are fixed at the special Wyckoff position 4*b* (½, 0, 0), while seven positional parameters of the atoms Pr(Ca), O1 [both at 4*c* (*x*, *y*, ¼)] and O2 [at 8*d* (*x*, *y*, *z*)] were allowed to vary during the refinements. Further, three lattice parameters (*a*, *b*, and *c*), seven profile function parameters (split pseudo-Voigt function), and three isotropic thermal parameters B_{is} were refined. The B_{is} values of the two oxygen atoms were constrained to be equal. A data set of $Pr_{0.85}Ca_{0.15}VO_3$ was collected at the larger wavelength $\lambda = 0.6976$ Å, where only 256 reflections were measured instead of 684 using $\lambda = 0.5037$ Å. Therefore, the standard deviations of the parameters of $Pr_{0.85}Ca_{0.15}VO_3$ were found to be somewhat enlarged. In Table I it can be seen that the positional and isotropic thermal parameters of the oxygen atoms do not reach the same accuracy as those of the Pr(Ca) site due to the smaller

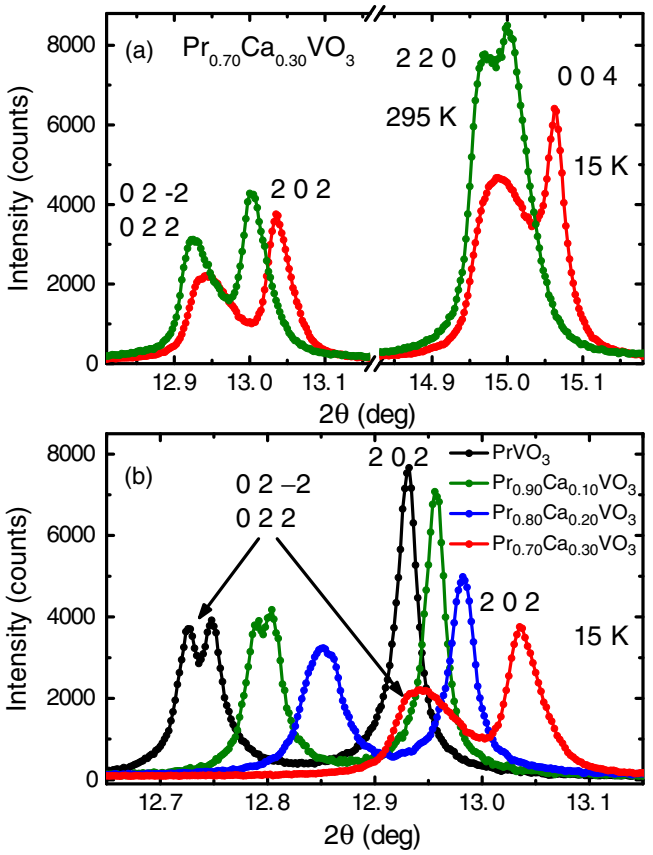

FIG. 4. Sections of synchrotron diffraction patterns of $Pr_{1-x}Ca_xVO_3$. (a) Comparison of the peak profiles of $Pr_{0.70}Ca_{0.30}VO_3$ measured at 15 and 295 K. At 15 K, a strongly anisotropic peak broadening was observed, where the linewidth (HWHM) of the reflection 220 shows the strongest increase. (b) Evolution of the monoclinic peak splitting in $Pr_{1-x}Ca_xVO_3$ with increasing Ca doping. For the insulating vanadates with $x = 0$, 0.10, and 0.20, the orthorhombic 022 reflection splits into the monoclinic reflections 022 and 02–2, respectively. With increasing Ca content, the monoclinic distortions are continuously weakened and disappear in the metallic state. However, the reflection pair 022/02–2 shows an asymmetrically broadened peak profile.

scattering power of the relatively light oxygen atoms in x-ray diffraction. Nevertheless, for all investigated vanadates, it was possible to determine the V-O bond distances in the VO_6 octahedra with good accuracy (Table I). The bond distances d(V-O1), d(V-O21), and d(V-O22) are almost identical, which confirms the absence of Jahn-Teller distortions at 295 K. Figure 5 presents the change of the averaged d(V-O) values up to $x = 0.30$. It is interesting to note that both the lattice parameters and V-O bond distances at room temperature show a slight decrease from the insulating to the metallic state without any significant anomaly at the metal-insulator transition. For $PrVO_3$ and $Pr_{0.70}Ca_{0.30}VO_3$, the averaged V-O bond distance changes from d_{av}(V-O) = 2.007(2) Å to d_{av}(V-O) = 1.974(2) Å. It can thus be concluded that the shrinking of the cell volume is strongly correlated with the reduction of the V-O bond lengths.

We now turn to the crystal structure in the low-temperature structural phase. For the parent compound $PrVO_3$, a strong monoclinic splitting is observed at 15 K in the orthorhombic reflection 022, while the reflection 202 remains almost unchanged (Fig. 4). The same type of splitting was observed earlier for $LaVO_3$ and $CeVO_3$, where the crystal structure was successfully refined in the monoclinic space group $P2_1/b$ ($P2_1/b$ 1 1, No 14) [16,23]. For all insulating samples, Rietveld refinements were therefore performed in the group $P2_1/b$. Due to the lower symmetry, the collected synchrotron powder patterns contained a larger number (about 1300 reflections) than at room temperature. In this space group, the vanadium site is split into the special Wyckoff positions 2c (½, 0, 0) and 2d (½, 0, ½), respectively. The eightfold O2 sites (8d in $Pbnm$) split into two fourfold general positions: O2 and O3, both in 4e (x, y, z) of $P2_1/b$. The Pr (Ca) and O1 atoms are also located at the Wyckoff position 4e. In this structure, a total of 12 positional parameters could be refined, resulting in a residual of $R_F \leqslant 0.027$. The refinements show that the z parameters of the Pr (Ca) and O1 atoms are very close to the ideal value of ¼. Therefore, in the last refinement, these two z values were fixed to be equal to ¼.

The splitting into the reflections 022 and 02–2 (in $Pbnm$) indicates that the monoclinic plane is the bc plane (or b-glide plane of $Pbnm$) so that the monoclinic angle is α. At 15 K, the monoclinic angle of pure $PrVO_3$ reaches the value $\alpha = 90.1116(3)^\circ$. For the isotypic vanadates $LaVO_3$ and YVO_3, where the ionic radii $r(La^{3+})$ and $r(Y^{3+})$ are larger and smaller than $r(Pr^{3+})$, respectively, the monoclinic angles were found to be $\alpha = 90.1251(4)^\circ$ (at 100 K) and $\alpha = 90.020(3)^\circ$ (at 85 K) [15,23]. This shows that the deviation from the ideal value of 90° decreases significantly with the size of the R^{3+} ions. Taking into account the trend $r(La^{3+}) > r(Ce^{3+}) > r(Pr^{3+})$, one should accordingly expect a monoclinic angle for $CeVO_3$ larger than $\alpha = 90.1116(3)^\circ$ of $PrVO_3$. Interestingly, for $CeVO_3$, a considerably smaller value $\alpha = 90.0798(3)^\circ$ was found [16]. Anomalies were also found for this vanadate regarding the cell volumes as well as the structural and magnetic phase transition temperatures [9,15,16]. Indeed, cerium ions in intermetallic materials are well known to appear also in tetravalent, intermediate, or mixed-valent states. Our present paper, therefore, confirms that such valence states can also exist in Mott-Hubbard insulators such as $CeVO_3$ [16]. Further, we can conclude that a charge transfer occurs not only between the V and O atoms, as discussed above, but also between the Ce^{n+} ions and the VO_6 octahedra. In contrast, this behavior is not observed for trivalent R^{3+} ions such as La^{3+} and Pr^{3+}, where the valence of 3+ is well stabilized.

We now discuss the modification of the monoclinic structure in $Pr_{1-x}Ca_xVO_3$ from the insulating to the metallic state. Figure 4(b) shows that the monoclinic splitting of the reflection 022 decreases continuously with increasing Ca content. This trend was confirmed by the Rietveld refinements of the 15 K data, where the monoclinic angle $\alpha = 90.0770(6)^\circ$ of the still insulating vanadate $Pr_{0.80}Ca_{0.20}VO_3$ was found to be significantly closer to 90° than the value $\alpha = 90.1116(3)^\circ$ of undoped $PrVO_3$. The positional parameters and V-O bond distances are listed in Table I. Even for the vanadium atoms V1 and V2 located at different sites, one finds similar V-O bond distances: d(V1-O11) ≅ d(V2-O12), d(V1-O21) ≅ d(V2-O31), and d(V1-O22) ≅ d(V2-O32). In the lower panel of Fig. 5, we therefore present the averaged

TABLE I. Results of the Rietveld refinements of $Pr_{1-x}Ca_xVO_3$. For the synchrotron powder data collected at 15 K and 295 K, the crystal structures were refined in the monoclinic and orthorhombic space groups $P2_1/b$ and *Pbnm*, respectively. Cell parameters and interatomic distances in the VO_6 octahedra (in Å) are listed. The isotropic thermal parameters B (in Å^2) of the O atoms were constrained to be equal, as well as those of the two V atoms in the space group $P2_1/b$. Using this space group, the parameters z(Pr/Ca) and z(O1) were set to 0.25. The given residual is given as $R_F = \sum \|F_{obs}| - |F_{cal}\| / \sum |F_{obs}|$.

	$PrVO_3$		$Pr_{0.90}Ca_{0.10}VO_3$		$Pr_{0.85}Ca_{0.15}VO_3$		$Pr_{0.80}Ca_{0.20}VO_3$		$Pr_{0.70}Ca_{0.30}VO_3$	
Space gr.	15 K $P2_1/b$	295 K *Pbnm*	15 K $P2_1/b$	295 K *Pbnm*	15 K $P2_1/b$	295 K *Pbnm*	15 K $P2_1/b$	295 K *Pbnm*	15 K *Pbnm*	295 K *Pbnm*
a [Å]	5.48231(2)	5.48394(2)	5.46591(3)	5.46873(2)	5.45839(2)	5.46432(8)	5.45091(3)	5.45739(3)	5.43047(3)	5.44568(6)
b [Å]	5.60862(2)	5.57168(2)	5.56888(3)	5.54170(2)	5.55091(2)	5.52890(8)	5.53397(3)	5.51875(3)	5.48962(3)	5.49457(6)
c [Å]	7.69108(3)	7.77294(3)	7.69039(4)	7.75111(2)	7.68986(3)	7.74414(12)	7.68848(5)	7.73440(4)	7.68507(3)	7.71520(9)
α [°]	90.1116(3)	90	90.0798(4)	90	90.0773(3)	90	90.0771(6)	90	90	90
V [Å^3]	236.486(2)	237.500(1)	234.086(2)	234.905(1)	232.995(2)	233.964(6)	231.924(2)	232.944(2)	229.101(2)	230.852(4)
x(Pr/Ca)	0.9891(1)	0.9913(1)	0.9908(1)	0.9920(1)	0.9908(1)	0.9925(2)	0.9921(1)	0.9928(1)	0.9942(1)	0.9937(1)
y(Pr/Ca)	0.0481(1)	0.0439(1)	0.0454(1)	0.0413(3)	0.0435(1)	0.0398(1)	0.0426(1)	0.0388(5)	0.0384(1)	0.0354(1)
z(Pr/Ca)	0.25	¼	0.25	¼	0.25	¼	0.25	¼	¼	¼
x (O1)	0.0848(4)	0.0833(6)	0.0806(6)	0.0783(4)	0.0813(5)	0.0773(14)	0.0794(5)	0.0773(7)	0.0723(8)	0.0681(8)
y (O1)	0.4780(5)	0.4831(5)	0.4820(5)	0.4836(4)	0.4834(5)	0.4810(10)	0.4827(4)	0.4850(5)	0.4855(5)	0.4827(5)
z (O1)	0.25	¼	0.25	¼	0.25	¼	0.25	¼	¼	¼
x (O2)	0.6955(13)	0.7073(4)	0.6991(16)	0.7092(3)	0.7015(15)	0.7087(11)	0.6999(16)	0.7116(5)	0.7105(5)	0.7102(5)
y (O2)	0.2806(9)	0.2937(4)	0.2822(12)	0.2909(3)	0.2851(11)	0.2885(10)	0.2816(12)	0.2934(5)	0.2899(5)	0.2873(5)
z (O2)	0.0451(8)	0.0426(3)	0.0435(10)	0.0396(2)	0.0427(9)	0.0384(7)	0.0411(11)	0.0369(4)	0.0383(3)	0.0378(4)
x (O3)	0.2854(13)	–	0.2802(15)	–	0.2861(15)	–	0.2790(16)	–	–	–
y (O3)	0.7000(9)	–	0.7006(12)	–	0.7036(11)	–	0.7061(13)	–	–	–
z (O3)	0.5436(8)	–	0.5430(10)	–	0.5394(9)	–	0.5408(11)	–	–	–
B_{is} (Pr/Ca)	0.349(3)	0.629(3)	0.403(4)	0.678(3)	0.266(3)	0.525(10)	0.242(3)	0.616(4)	0.312(3)	0.543(4)
B_{is} (V)	0.257(9)	0.392(9)	0.256(10)	0.406(7)	0.242(8)	0.249(23)	0.317(8)	0.509(11)	0.286(9)	0.379(10)
B_{is} (O)	0.65(4)	0.78(3)	0.55(4)	0.92(3)	0.48(3)	0.98(10)	0.51(3)	0.63(4)	0.70(4)	0.98(4)
R_F	0.0159	0.0210	0.0255	0.0175	0.0177	0.0181	0.0188	0.0257	0.0265	0.0238
$d_{V1\text{-}O11}$	1.9822(7)	1.9984(7)	1.9752(8)	1.9866(5)	1.9753(7)	1.9843(17)	1.9727(7)	1.9808(8)	1.9625(8)	1.9665(8)
$d_{V1\text{-}O21}$	1.935(6)	2.002(2)	1.940(7)	1.992(2)	1.955(5)	1.997(6)	1.927(7)	1.964(3)	1.972(3)	1.971(3)
$d_{V1\text{-}O22}$	2.103(6)	2.020(2)	2.071(8)	2.000(2)	2.040(5)	1.983(6)	2.059(8)	2.009(3)	1.981(8)	1.985(3)
$d_{V2\text{-}O12}$	1.9817(7)	–	1.9749(8)	–	1.9750(7)	–	1.9724(7)	–	–	–
$d_{V2\text{-}O31}$	1.954(6)	–	1.924(8)	–	1.957(6)	–	1.927(8)	–	–	–
$d_{V2\text{-}O32}$	2.081(6)	–	2.082(7)	–	2.041(5)	–	2.048(7)	–	–	–

bond lengths d_{av}(V-O1) = [d(V1-O11) + d(V2-O12)]/2, d_{av}(V-O2) = [d(V1-O21) + d(V2-O31)]/2, and d_{av}(V-O3) = [d(V1-O22) + d(V2-O32)]/2, respectively. The elongated V-O3 bond is decreasing in the range $0 \leqslant x \leqslant 0.20$, while the V-O1 and V-O2 bond distances remain almost unchanged. In $PrVO_3$, the elongated V-O3 bond distance reaches an average value of d_{av}(V-O3) = 2.092(6) Å, while the value d_{av}(V-O3) = 2.053(8) Å of the still insulting vanadate $Pr_{0.80}Ca_{0.20}VO_3$ is slightly larger than d_{av}(V-O1) and d_{av}(V-O2). This indicates that the Jahn-Teller distortion of the VO_6 octahedra (and, hence, orbital order) is well established in the insulating state, in agreement with the discussion in Sec. III A.

The monoclinic angle α decreases only slightly up to $x = 0.20$, followed by a sudden change at the IMT (Fig. 5). A structure refinement of metallic $Pr_{0.70}Ca_{0.30}VO_3$ in the monoclinic space group $P2_1/b$ resulted in a monoclinic angle $\alpha = 90.012(37)^\circ$, that is, the angle equals 90°, and the monoclinic splitting vanishes within the experimental error. The average crystal structure obtained from the integrated intensities of the Bragg reflections thus remains orthorhombic down to low temperature (Fig. 3), and all V-O bond distances are equal within the experimental error (Fig. 5). This confirms the quenching of orbital order already inferred from the absence of a structural phase transition in the metallic sample (Sec. III A).

The linewidth [half width at half maximum (HWHM)] of the Bragg reflections provides further information about the doping dependent spin and orbital correlations. For the insulating vanadates $PrVO_3$, $Pr_{0.90}Ca_{0.10}VO_3$, and $Pr_{0.85}Ca_{0.15}VO_3$, the peak profiles of all reflections are closely similar, isotropic, and consistent with the experimental resolution for the data sets collected at 15 and 295 K. For $Pr_{0.80}Ca_{0.20}VO_3$, which is close to the IMT, the data indicate a subtle broadening of some reflections at low temperature (Fig. 4). In metallic $Pr_{0.70}Ca_{0.30}VO_3$, the structural Bragg reflections clearly exhibit a strongly anisotropic broadening with decreasing temperature. Even at 295 K, the widths of the structural Bragg reflections are already slightly broader than the instrumental resolution, indicating either lattice strains or deviations from a random distribution of Ca substituents or a combination of both effects [Fig. 4(a)].

At 15 K, the 022 reflection, which is subject to monoclinic splitting in the insulating samples, was found to be broader than

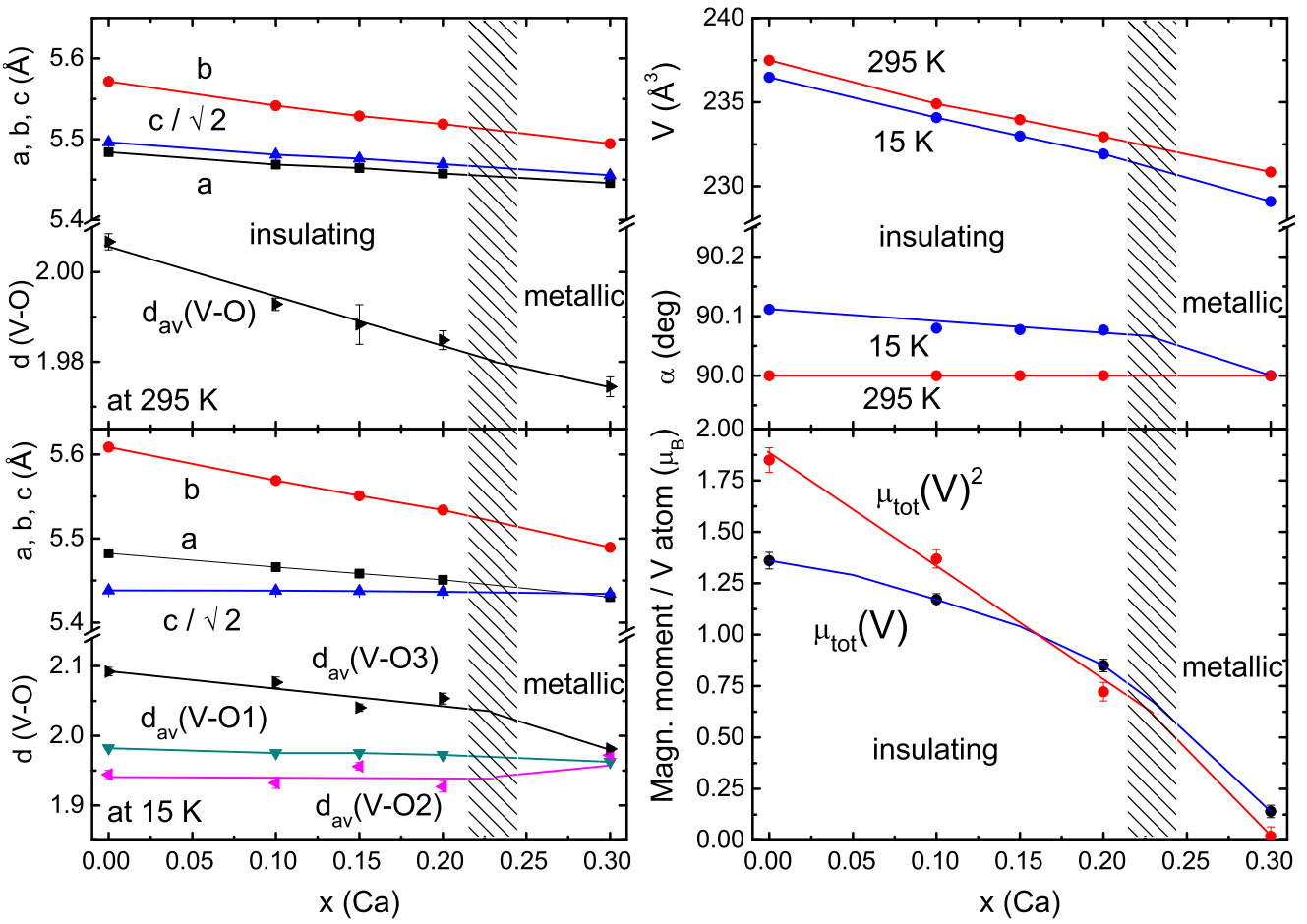

FIG. 5. Variation of lattice parameters and V-O bond distances in $Pr_{1-x}Ca_xVO_3$ at 15 and 295 K. The IMT is marked by the dashed area. For simplicity, the averaged V-O bond distances d_{av}(V-O) = $[d(\text{V-O11}) + d(\text{V-O21}) + d(\text{V-O22})]/3$ are shown for the orthorhombic structure at 295 K; in the case of the monoclinic structure, the averaged bond lengths are $d_{av}(\text{V-O1}) = [d(\text{V1-O11}) + d(\text{V2-O12})]/2$, $d_{av}(\text{V-O2}) = [d(\text{V1-O21}) + d(\text{V2-O31})]/2$, and $d_{av}(\text{V-O3}) = [d(\text{V1-O22}) + d(\text{V2-O32})]/2$, respectively (see text). Further, the variation of the magnetic moments μ_{tot} (and their square values μ^2_{tot}) of the V atoms is shown. The bold lines serve as guides to the eye.

202, which does not split in the monoclinic phase [Fig. 4(b)]. A comparison to the insulating samples indicates that the peak broadening cannot be ascribed to unresolved monoclinic distortions alone [Fig. 4(b)]. Rather, the reciprocal HWHM of the 002/02−2 reflection translates into a structural correlation length of ∼70 Å. Figure 4(a) shows that the trend of anisotropic peak broadening is even more pronounced for the reflections 220 and 004 (200 and 002 in the pseudocubic notation). We obtain identical results by synchrotron powder diffraction from two different samples of $Pr_{0.70}Ca_{0.30}VO_3$, confirming the macroscopic homogeneity of the samples. We therefore conclude that the observed anisotropic peak broadening in $Pr_{0.70}Ca_{0.30}VO_3$, which predominantly appears in the *ab* plane, arises mainly from strain due to short-range orbital order. Our Rietveld refinements of the powder pattern collected at 15 K indeed resulted in satisfactory peak fits in the orthorhombic space group *Pbnm* using an anisotropic strain model provided by the *FullProf* program (see Ref. [33]), hence supporting the suggestion that the anisotropic broadening is caused by local distortions of the VO_6 octahedra in the *ab* plane. Similar effects were found recently in the solid solution series $Ni_{1-x}Cu_xCr_2O_4$, where an anisotropic peak broadening of particular Bragg reflections was observed as a consequence of competing Jahn-Teller effects acting along different axes [37]. For this compound, high-resolution synchrotron diffraction data also excluded a lowering of the average crystal structure symmetry.

C. Magnetic ordering

The magnetic ordering of the vanadium and praseodymium ions was investigated by single-crystal neutron diffraction. The experiments showed that our single crystals of the insulating vanadates $Pr_{0.90}Ca_{0.10}VO_3$ and $Pr_{0.80}Ca_{0.20}VO_3$ were untwinned so that we were able to give a detailed picture of the spin ordering for these two systems. The total magnetic moments of the V and Pr atoms, as well as their components along the crystallographic axes, could be deduced from the magnetic intensities of the characteristic reflections 100, 010, 102, 012, 200, 020, and 002. Figure 6 shows the temperature dependence of these reflections for $Pr_{0.90}Ca_{0.10}VO_3$. The reflections 100, 010, 102, and 012 exhibit a spontaneous increase in their magnetic intensity at the Néel temperature $T_N = 117(2)$ K, indicating the onset

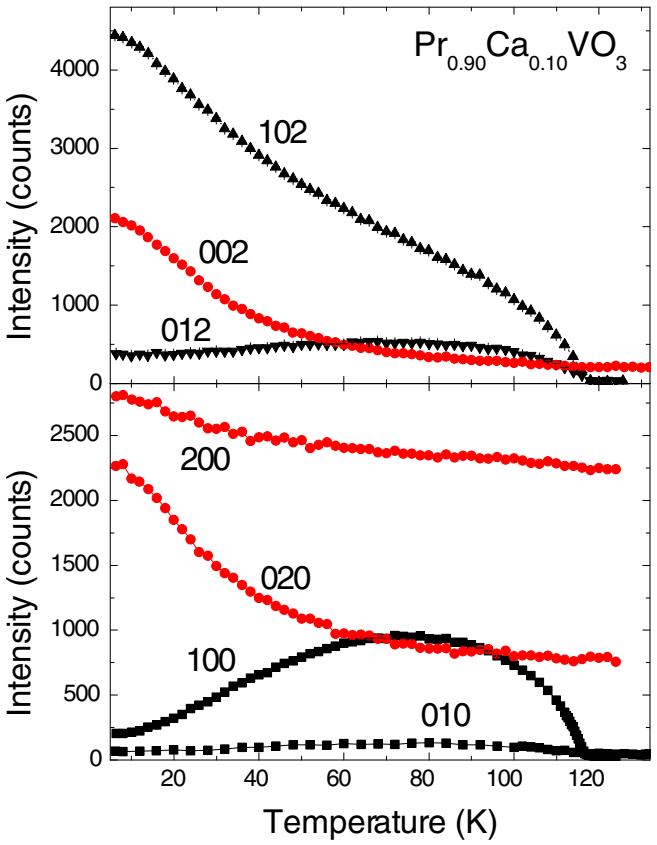

FIG. 6. Temperature dependence of magnetic Bragg intensities of $Pr_{0.90}Ca_{0.10}VO_3$. The reflections 100, 010, 012, and 102 show a spontaneous intensity increase below $T_N = 117$ K due to the onset of a C-type order of the vanadium moments. The decrease of the intensities of 010, 100, and 012, as well as the increase of the 102 below about 60 K, indicate the onset of a superimposed induced C-type ordering of the praseodymium moments at lower temperature. Further, the increase of magnetic intensity of the reflections 200, 020, and 002 indicates an induced ferromagnetic moment of the praseodymium ions.

of C-type antiferromagnetic spin ordering of the vanadium sublattice. The V-atoms located at the positions ½, 0, 0; ½, 0, ½; 0, ½, 0; 0, ½, ½ show the spin sequence $++--$. The intensity ratios $I(100)/I(010)$ and $I(102)/I(012)$ of $Pr_{0.90}Ca_{0.10}VO_3$ are similar to those observed earlier for $CeVO_3$ [17]. Our data analysis showed that the vanadium moments in $Pr_{0.90}Ca_{0.10}VO_3$ are aligned within the ab plane and that the C_y component is the strongest.

Upon cooling down to 10 K, the intensities of these reflections exhibit a nonmonotonic temperature dependence, which is analogous to the behavior of $CeVO_3$ [16]. This can be ascribed to the influence of the lanthanide moments, which are polarized in the presence of the exchange field produced by the antiferromagnetic vanadium sublattice, resulting in a magnetic structure with the same symmetry [15]. The magnetic order of the praseodymium sublattice is a superposition of C_x and C_y modes. Figure 6 shows that additional magnetic intensity also appears on the reflections 200, 020, and 002, indicating a coexisting ferromagnetic order of the Pr^{3+} ions. The ferromagnetic components are also oriented in the

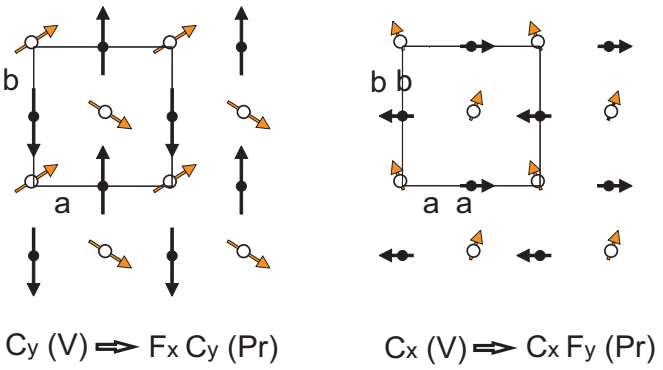

FIG. 7. Magnetic structure of $Pr_{0.90}Ca_{0.10}VO_3$ at 15 K. The open circles represent the praseodymium and the smaller filled circles the vanadium ions. The praseodymium atoms are located at $z = 1/4$, while the vanadium atoms are at $z = 0$ and $z = 1/2$, respectively. The magnetic moments of the metal atoms are aligned within the ab plane. Along the c axis, all the moments are coupled ferromagnetically. For clarity, the magnitude of the C_x component of the praseodymium moment is somewhat exaggerated.

ab plane. In the orthorhombic space group $Pbnm$, the Pr atoms are located at the special Wyckoff position 4c: (1) x, y, ¼; (2) $-x$, $-y$, ¾; (3) $\frac{1}{2} - x$, $\frac{1}{2} + y$, ¼; (4) $\frac{1}{2} + x$, $\frac{1}{2} - y$, ¾. In the lower symmetry of $P2_1/b$, the Pr atoms are located at the same positions, with the difference that now the z parameter ($z \approx 1/4$) of the general position 4e can be varied. However, the refinement of the crystal structure resulted in a value very close to $z = 1/4$, indicating that the magnetic ordering is still compatible with the symmetry of $Pbnm$. Possible magnetic structures can be theoretically deduced from Bertaut's representation analysis [38]. It was shown for both $P2_1/b$ and $Pbnm$ that the magnetic ordering in the ab plane can be described with the basis vectors (C_x, F_y) and (F_x, C_y), defined as $F(++++)$ and $C(++--)$. This allows coexistence of a C- and F-type ordering of the Pr moments, as shown in Fig. 7 [15].

For the refinement of the magnetic structure of $PrVO_3$, $Pr_{0.90}Ca_{0.10}VO_3$, and $Pr_{0.80}Ca_{0.20}VO_3$, we used the magnetic intensities of the reflections 100, 010, 102, 012, 104, 014, 200, 020, and 002. As already mentioned above, the individual magnetic components of both the V and Pr atoms could only be determined from the data sets of $Pr_{0.90}Ca_{0.10}VO_3$ and $Pr_{0.80}Ca_{0.20}VO_3$, where untwinned single crystals were available. The magnetic components within the ab plane as well as the total moments of the V and Pr atoms obtained at 10 K are listed in Table II, and the temperature dependence of the magnetic moments is presented in Fig. 8. For the end member $PrVO_3$, we determined only the total magnetic moments of the V and Pr atoms at 10 K. Our data analysis showed that the overall magnetic structure in $Pr_{1-x}Ca_xVO_3$ does not change with increasing Ca content and that the ratios of the vanadium and praseodymium moments are similar throughout the series. This is consistent with the notion that exchange interactions between the ordered vanadium moments and the paramagnetic praseodymium moments induce partial magnetic order on the Pr sublattice. On the other hand, hole doping results in a reduction of the magnetic moments of the V atoms. For the insulating vanadates $PrVO_3$, $Pr_{0.90}Ca_{0.10}VO_3$, and

TABLE II. Magnetic moments of the V- and Pr-atoms in $Pr_{0.90}Ca_{0.10}VO_3$ and $Pr_{0.80}Ca_{0.20}VO_3$ at 10 K as obtained from the refinements using our single-crystal neutron diffraction data. The Pr atoms are located at the positions (1) x, y, ¼; (2) $-x$, $-y$, ¾; (3) ½ − x, ½ + y, ¼; (4) ½ + x, ½ − y, ¾; while the V atoms are at (1) ½, 0, 0; (2) ½, 0, ½; (3) 0, ½, 0; and (4) 0, ½, ½, respectively.

	$Pr_{0.90}Ca_{0.10}VO_3$				$Pr_{0.80}Ca_{0.20}VO_3$			
Position	μ_x(Pr) [μ_B]	μ_y(Pr) [μ_B]	μ_x(V) [μ_B]	μ_y(V) [μ_B]	μ_x(Pr) [μ_B]	μ_y(Pr) [μ_B]	μ_x(V) [μ_B]	μ_y(V) [μ_B]
(1)	−0.17(2)	+0.43(2)	+0.33(3)		−0.06(2)	+0.42(2)	+0.22(3)	
(2)	−0.17(2)	+0.43(2)	+0.33(3)		−0.06(2)	+0.42(2)	+0.22(3)	
(3)	+0.17(2)	+0.43(2)	−0.33(3)		+0.06(2)	+0.42(2)	−0.22(3)	
(4)	+0.17(2)	+0.43(2)	−0.33(3)		+0.06(2)	+0.42(2)	−0.22(3)	
(1)	+1.10(3)	+0.73(2)		+1.12(3)	+0.90(3)	+0.57(2)		+0.82(3)
(2)	+1.10(3)	+0.73(2)		+1.12(3)	+0.90(3)	+0.57(2)		+0.82(3)
(3)	+1.10(3)	−0.73(2)		−1.12(3)	+0.90(3)	−0.57(2)		−0.82(3)
(4)	+1.10(3)	−0.73(2)		−1.12(3)	+0.90(3)	−0.57(2)		−0.82(3)

$Pr_{0.80}Ca_{0.20}VO_3$, we determined the total moments $\mu_{tot}(V) = 1.36(4)\ \mu_B$, $1.17(3)\ \mu_B$, and $0.85(3)\ \mu_B$, respectively.

Interestingly, for the metallic vanadate $Pr_{0.70}Ca_{0.30}VO_3$, we still found very weak magnetic intensities on the reflections 100 and 010 below about 60 K (see Fig. 3). The integrated intensities of these reflections at low temperature give a weak ordered moment of the vanadium atoms of $\mu_{tot}(V) = 0.14(3)\ \mu_B$. The spin correlation length, as determined from the

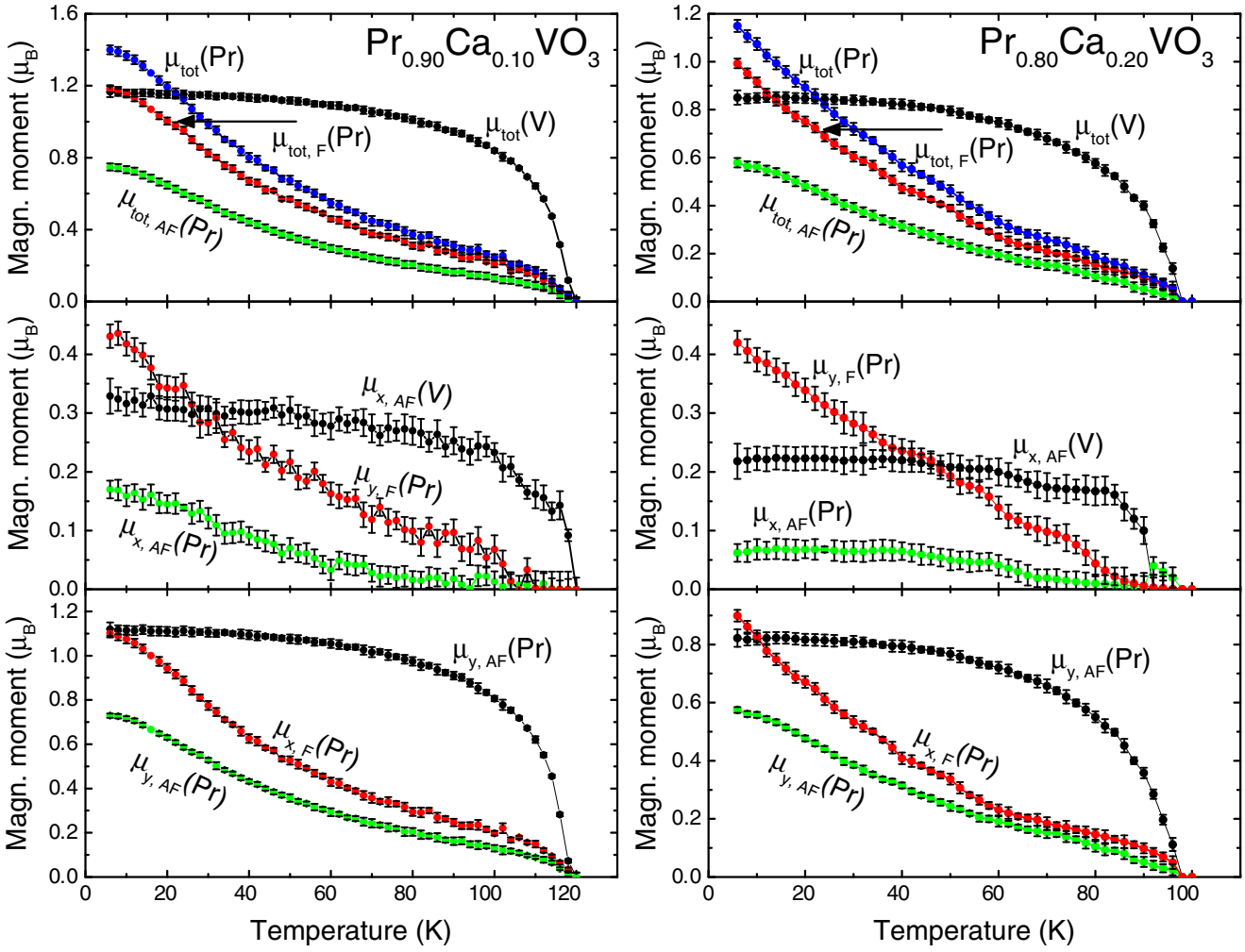

FIG. 8. Temperature dependence of the ordered magnetic moments of the praseodymium and vanadium atoms in $Pr_{0.90}Ca_{0.10}VO_3$ and $Pr_{0.80}Ca_{0.20}VO_3$. Below the Néel temperatures $T_N = 117$ and 95 K, respectively, the C-type magnetic order of the vanadium moments sets in spontaneously. The ordered vanadium sublattice induces a polarization of the praseodymium moments via Pr-V exchange, resulting in a ferrimagnetic structure.

linewidth of the antiferromagnetic Bragg reflection 100, drops to ∼18 Å in the metallic phase, which is a direct indication of spin-orbital disorder in this phase. The magnetic order parameter may originate from nm-sized regions in which both the concentration of Ca atoms and the concentration of mobile hole is reduced. However, the onset of static antiferromagnetic short-range order below 60 K results in a pronounced upturn in the resistivity of metallic $Pr_{1-x}Ca_xVO_3$, as observed by Fujioka *et al.* [10], which rules out macroscopic phase separation or concentration gradients.

In Fig. 5, where the moments $\mu_{tot}(V)$ are plotted as a function of x, it can be seen that the decrease of the moments is more pronounced than the decrease of the lattice parameters and V-O bond lengths. Interestingly, the plotted square values $\mu_{tot}(V)^2$ show a linear decrease in the insulating range $0 \leqslant x \leqslant 0.20$. The total saturation moments of the Pr atoms of the insulating vanadates $PrVO_3$, $Pr_{0.90}Ca_{0.10}VO_3$, and $Pr_{0.80}Ca_{0.20}VO_3$ were found to be $\mu_{tot}(Pr) = 1.62(4)\,\mu_B$, $1.40(3)\,\mu_B$, and $1.15(3)\,\mu_B$, respectively. These values are larger than those of the V atoms but are still considerably smaller than the theoretically expected moment of the Pr^{3+} ion with $g\,J = 3.20\,\mu_B$ (electron configuration $4f^2$, $J = 4$). This demonstrates that the moments of the Pr^{3+} ions are partially polarized only at 10 K in the presence of the exchange field induced by the antiferromagnetically ordered vanadium sublattice.

IV. CONCLUSIONS

The combination of high-resolution x-ray powder diffraction and single-crystal neutron diffraction has provided detailed insight into the influence of hole doping on spin and orbital ordering in $Pr_{1-x}Ca_xVO_3$, a compound that is suitable as a model system in view of the closely similar ionic radii of the Ca^{2+} and Pr^{3+} ions. $PrVO_3$, the Mott-insulating end member of the series, displays a sequence of orbital and magnetic ordering transitions analogous to other insulating orthovanadates. For doping levels below the IMT, long-range orbital and magnetic order persists, albeit with reduced transition temperatures. In the metallic phase, anisotropic broadening of lattice Bragg reflections indicates enhanced lattice strain associated with short-range orbital correlations and magnetic neutron scattering uncovered manifestations of antiferromagnetic short-range order.

These observations indicate a key role of spin and orbital correlations in the IMT, which has been anticipated by prior experimental and theoretical work. In addition to the conventional charge-lattice coupling, a doped hole in an orbitally degenerate Mott insulator may generate strong local distortions through the modification of the spin-orbital structure in its neighborhood, forming a polaron with large binding energy [28–30,32,39,40]. Its enhanced effective mass reduces the mobility and leads to the localization of carriers in the random potential of dopant ions. The role of polarons in the metal-insulator transition was extensively discussed in the context of doped $R_{1-x}A_xMnO_3$, where A is divalent alkaline-earth element [32,39,40]. In the case of doped vanadates such as $Pr_{1-x}Ca_xVO_3$, two electrons are located in the t_{2g} orbital level. Upon doping with Ca^{2+}-ions, holes injected into the system couple simultaneously to the C-type antiferromagnetic and G-type orbital order, forming spin-orbital polarons. Their localization results in random strain fields, which degrade the orbital and magnetic long-range order and prohibit the formation of a conducting state at low doping concentrations. Isolated polarons generate incoherent diffuse scattering in insulating vanadates (see Ref. [41]) but do not significantly affect the Bragg reflections studied in our crystallographic analysis. A direct observation of lattice polaron formation in the local structure of $La_{1-x}Ca_xMnO_3$ was reported earlier [42].

Upon crossing the IMT at $x = 0.23$, however, the polarons start to overlap. As a consequence, their binding energy decreases, coherent electronic bands are formed, and the conductivity is enhanced. At the same time, the overlapping polarons generate a coherent strain field that can be clearly recognized in marked changes of the momentum widths of selected lattice Bragg reflections across the IMT. Below ∼60 K, the metallic sample $Pr_{0.7}Ca_{0.3}VO_3$ orders magnetically, consistent with increase in resistivity observed by Fujioka *et al.* [10] in metallic $Pr_{1-x}Ca_xVO_3$ close to the IMT.

Our data thus provide indirect evidence for the formation and percolation of spin-orbital polarons in $Pr_{1-x}Ca_xVO_3$ and underline their key role in the IMT. Further studies will be necessary to give a more detailed description of the lattice microstructure as well as structural and electronic short-range order in the metallic state.

ACKNOWLEDGMENTS

We acknowledge financial support from the Deutsche Forschungsgemeinschaft (DFG) under Grant No. TRR80 and from the Australian Research Council through Grant No. ARC-DP110105346.

[1] For a review, see S. Maekawa, T. Tohyama, S. E. Barnes, S. Ishihara, W. Koshibae, and G. Khaliullin, *Physics in Transition Metal Oxides* (Springer-Verlag, Berlin, 2004).

[2] G. Khaliullin, Prog. Theor. Phys. Suppl. **160**, 155 (2005).

[3] C. Ulrich, G. Khaliullin, J. Sirker, M. Reehuis, M. Ohl, S. Miyasaka, Y. Tokura, and B. Keimer, Phys. Rev. Lett. **91**, 257202 (2003).

[4] Y. Ren, T. T. M. Palstra, D. I. Khomskii, E. Pellegrin, A. A. Nugroho, A. A. Menovsky, and G. A. Sawatzky, Nature **396**, 441 (1998).

[5] G. R. Blake, T. T. M. Palstra, Y. Ren, A. A. Nugroho, and A. A. Menovsky, Phys. Rev. Lett. **87**, 245501 (2001); Phys. Rev. B **65**, 174112 (2002).

[6] H. Kawano, H. Yoshizawa, and Y. Ueda, J. Phys. Soc. Jpn. **63**, 2857 (1994).

[7] H. C. Nguyen and J. B. Goodenough, Phys. Rev. B **52**, 324 (1995).

[8] S. Miyasaka, T. Okuda, and Y. Tokura, Phys. Rev. Lett. **85**, 5388 (2000).

[9] S. Miyasaka, Y. Okimoto, M. Iwama, and Y. Tokura, Phys. Rev. B **68**, 100406(R) (2003).

[10] J. Fujioka, S. Miyasaka, and Y. Tokura, Phys. Rev. B **72**, 024460 (2005).
[11] J. Fujioka, S. Miyasaka, and Y. Tokura, Phys. Rev. Lett. **97**, 196401 (2006).
[12] J. Fujioka, S. Miyasaka, and Y. Tokura, Phys. Rev. B **77**, 144402 (2008).
[13] J. Fujioka, T. Yasue, S. Miyasaka, Y. Yamasaki, T. Arima, H. Sagayama, T. Inami, K. Ishii, and Y. Tokura, Phys. Rev. B **82**, 144425 (2010).
[14] A. A. Tsvetkov, F. P. Mena, P. H. M. van Loosdrecht, D. van der Marel, Y. Ren, A. A. Nugroho, A. A. Menovsky, I. S. Elfimov, and G. A. Sawatzky, Phys. Rev. B **69**, 075110 (2004).
[15] M. Reehuis, C. Ulrich, P. Pattison, B. Ouladdiaf, M. C. Rheinstädter, M. Ohl, L. P. Regnault, M. Miyasaka, Y. Tokura, and B. Keimer, Phys. Rev. B **73**, 094440 (2006).
[16] M. Reehuis, C. Ulrich, P. Pattison, M. Miyasaka, Y. Tokura, and B. Keimer, Eur. Phys. J. B **64**, 27 (2008).
[17] M. Reehuis, C. Ulrich, K. Prokeš, S. Mat'aš, J. Fujioka, S. Miyasaka, Y. Tokura, and B. Keimer, Phys. Rev. B **83**, 064404 (2011).
[18] J.-Q. Yan, J.-S. Zhou, J. B. Goodenough, Y. Ren, J. G. Cheng, S. Chang, J. Zarestky, O. Garlea, A. Llobet, H. D. Zhou, Y. Sui, W. H. Su, and R. J. McQueeney, Phys. Rev. Lett. **99**, 197201 (2007).
[19] Z. Fang and N. Nagaosa, Phys. Rev. Lett. **93**, 176404 (2004).
[20] A. M. Oleś, P. Horsch, and G. Khaliullin, Phys. Rev. B **75**, 184434 (2007).
[21] S. Geller, Acta Cryst. **10**, 243 (1957).
[22] S. Geller, J. Chem. Phys. **24**, 1236 (1956).
[23] P. Bordet, C. Chaillout, M. Marezio, Q. Huang, A. Santoro, S.-W. Cheong, H. Takagi, C. S. Oglesby, and B. Batlogg, J. Solid State Chem. **106**, 253 (1993).
[24] M. J. Martínez-Lope, J. A. Alonso, M. Retuerto, and M. T. Fernández-Diaz, Inorg. Chem. **47**, 2634 (2008).
[25] P. Horsch, A. M. Oleś, L. F. Feiner, and G. Khaliullin, Phys. Rev. Lett. **100**, 167205 (2008).
[26] H. F. Pen, M. Abbate, A. Fujimori, Y. Tokura, H. Eisaki, S. Uchida, and G. A. Sawatzky, Phys. Rev. B **59**, 7422 (1999).
[27] M. H. Sage, G. R. Blake, and T. T. M. Palstra, Phys. Rev. B **77**, 155121 (2008).
[28] P. Horsch and A. M. Olés, Phys. Rev. B **84**, 064429 (2011).
[29] A. Avella, P. Horsch, and A. M. Olés, Phys. Rev. B **87**, 045132 (2013).
[30] A. Avella, A. M. Olés, and P. Horsch, Phys. Rev. Lett. **115**, 206403 (2015).
[31] R. D. Shannon, Acta Crystallogr. Sect. A **32**, 751 (1976).
[32] R. Kilian and G. Khaliullin, Phys. Rev. B **60**, 13458 (1999).
[33] J. Rodríguez-Carvajal, Physica B **192**, 55 (1993).
[34] Edited by S. R. Hall, G. S. D. King, and J. M. Stewart, *Xtal 3.4 User's Manual* (University of Western Australia, Perth, 1995).
[35] V. F. Sears, in *International Tables for Crystallography*, edited by A. J. C. Wilson (Kluwer Academic Publishers, Dordrecht, 1995), Vol. C, p. 383.
[36] P. J. Brown, in *International Tables for Crystallography*, edited by A. J. C. Wilson (Kluwer Academic Publishers, Dordrecht, 1995), Vol. C, p. 391.
[37] M. Reehuis, M. Tovar, D. M. Többens, P. Pattison, A. Hoser, and B. Lake, Phys. Rev. B **91**, 024407 (2015).
[38] E. F. Bertaut, Acta Crystallogr. Sect. A **24**, 217 (1968).
[39] A. J. Millis, R. Mueller, and B. I. Shraiman, Phys. Rev. B **54**, 5389 (1996).
[40] D. I. Khomskii and G. A. Sawatzky, Solid State Commun. **102**, 87 (1997).
[41] S. Yano, D. Louca, J. C. Neuefeind, J.-Q. Yan, J.-S. Zhou, and J. B. Goodenough, Phys. Rev. B **90**, 214111 (2014).
[42] S. J. L. Billinge, R. G. DiFrancesco, G. H. Kwei, J. J. Neumeier, and J. D. Thompson, Phys. Rev. Lett. **77**, 715 (1996).